Geomechanics and Engineering, *Vol. 21, No. 5 (2020) 489-501*
DOI: https://doi.org/10.12989/gae.2020.21.5.489

Numerical simulation of set-up around shaft of XCC pile in clay

Fei Liu[1], Jiangtao Yi[1], Po Cheng[1] and Kai Yao*[2,3]

[1]*School of Civil Engineering, Chongqing University, No.83 Shabei Street, Chongqing, 400045, China*
[2]*School of Qilu Transportation, Shandong University, 12550 East Second Ring Road, Jinan, 250002, China*
[3]*Department of Civil and Environmental Engineering, National University of Singapore, 1 Engineering Drive 2, Singapore, 117576, Singapore*

(Received March 14, 2020, Revised April 22, 2020, Accepted April 24, 2020)

Abstract. This paper conducts a complicated coupled effective stress analysis of X-section-in-place concrete (XCC) pile installation and consolidation processes using the dual-stage Eulerian-Lagrangian (DSEL) technique incorporating the modified Cam-clay model. The numerical model is verified by centrifuge data and field test results. The main objective of this study is to investigate the shape effect of XCC pile cross-section on radial total stress, excess pore pressure and time-dependent strength. The discrepancies of the penetration mechanism and set-up effects on pile shaft resistance between the XCC pile and circular pile are discussed. Particular attention is placed on the time-dependent strength around the XCC pile shaft. The results show that soil strength improved more significantly close to the flat side compared with the concave side. Additionally, the computed ultimate shaft resistance of XCC pile incorporating set-up effects is 1.45 times that of the circular pile. The present findings are likely helpful in facilitating the incorporation of set-up effects into XCC pile design practices.

Keywords: XCC pile; coupled effective stress analysis; large deformation; time-dependent strength; pile shaft resistance

1. Introduction

Recently, a new-type of non-circular cross-sectional shaped pile, namely the X-section cast-in-place concrete (XCC) pile shown in Fig. 1(a), is developed in China (Lv *et al*. 2012, Liu *et al*. 2014, Kong *et al*. 2015, Sun *et al*. 2017). This new type of pile is widely used to reinforce soft ground in highway and railway construction. The XCC pile cross-section is designed as “X” shape, and its cross-sectional perimeter is larger than that of conventional circular pile with the same cross-sectional area, which in turn increases the XCC pile’s side surface area and side resistance (Lv *et al*. 2014a, b). As shown in Fig. 1(b), the XCC pile cross-section is composed of four flat sides and four concave sides. Three parameters including outsourcing diameter α, open arc *b*, and open arc angle θ_0 are used for controlling the size and shape of the XCC pile cross-section. As a cast-in-place pile, the key procedure for installation process includes (a) installing the pile mold with pile shoe in soft soil to form an X-shaped cavity (see Fig. 2), (b) pouring concrete into mold to create an X-shaped pile solid and then (c) uplifting the pile mold. When an XCC pile is installed into saturated clay, the soil around the XCC pile is left in a distressed state to accommodate the driving of XCC pile (Zhou *et al*. 2018, Ding *et al*. 2020). Over times, the excess pore pressure induced by the XCC pile installation progressively dissipates, followed by gradually recovery and enhancement of soil strength. Because the load-settlement response of an axially loaded pile heavily relies on strength of surrounding soil (Li *et al*. 2019), the XCC pile resistance exhibits apparently a time-dependent character after pile installation, commonly known as pile set-up. If the set-up effect is properly considered, economical design of XCC pile can be obtained

(a)

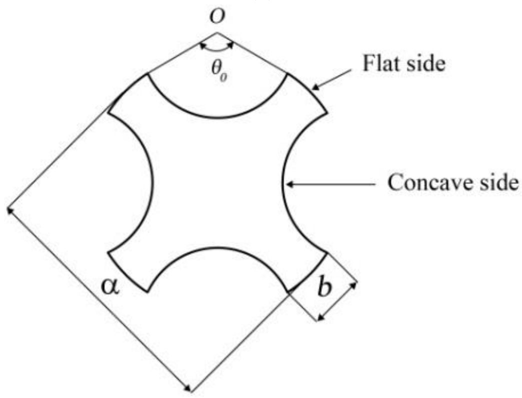

(b)

Fig. 1 Typical XCC pile in field: (a) XCC pile head and (b) XCC pile cross section (Zhou *et al*. 2019)

*Corresponding author, Ph.D.
E-mail: yaokai@u.nus.edu

http://www.techno-press.org/?journal=gae&subpage=7
ISSN: 2005-307X (Print), 2092-6219 (Online)

(a)

(b)

Fig. 2 Installation equipment: (a) X-section pile mold and (b) conical shoe with X cross section (Zhou *et al*. 2019)

by decreasing the pile diameter and length as well as the number of piles (Li *et al*. 2017b). To date, most of the previous work on XCC piles has focused on the stress transfer mechanism under vertical load and the installation effect (Lv *et al*. 2014a, b, 2018, Zhang *et al*. 2015, Zhou *et al*. 2019), while little research about the time-dependent soil behavior has been conducted, which is one of the most important considerations of XCC pile design. Besides, numerical works in this regard remain remarkably insufficient for XCC pile.

Although the finite element methods have versatility to solve a variety of geotechnical problems including those coupled with fluid flow (Yi *et al*. 2012, 2014, Azari *et al*. 2015, Hamann *et al*. 2015, Lorenzo *et al*. 2016, Wang *et al*. 2016), it is still a great challenge to simulate the entire 'installation-consolidation' process of an XCC pile in clayey soil, which involves large deformation, soil consolidation and pile geometry behavior, and their combination increases the complexity of analyzing such problems. For the small strain finite element methods coupled with effective stress, e.g., the Press-Replace Method (Lim *et al*. 2018) and expansion of cylindrical cavities (Rezania *et al*. 2017), there is no obstacle to simulate the two-dimensional (2D) axisymmetric geotechnical problems. However, many of the three-dimensional (3D) problems don't enjoy any symmetry, for example of the installation of an XCC pile. Therefore, these small strain finite element methods do not apply to such problems. Realistic modelling of XCC pile installation and subsequent consolidation process requires the aid of 3D effective stress large deformation analysis techniques, such as those techniques developed by Yi *et al.* (2012, 2014), Ceccato *et al.* (2016), Ullah *et al.* (2018). To date, however, the applications of these modelling methods have been restricted to relatively simple geotechnical problems such as the penetration and consolidation of cones with axisymmetric boundary condition and artificially modified geometry profile, like installation of spudcan foundations (Yi *et al*. 2012, 2014, Wang *et al*. 2016). Such complicated problems like modelling analysis of XCC pile are rarely reported.

This paper reports a coupled effective stress large deformation analysis of XCC pile installation and subsequent consolidation processes. The objectives of this paper are 1) to demonstrate the validity of DSEL computed technique to model XCC pile installation and consolidation process in clayey soil; 2) to analyze the installation mechanism of XCC pile and clarify the difference in the development of radial total stress and excess pore pressure between a circular pile and an XCC pile; 3) to quantify the magnitude and extend of soil strength enhancement around the XCC pile; 4) to evaluate the set-up effects on XCC pile shaft resistance arising from soil strength improvement.

2. Numerical modelling methodology

2.1 Dual-stage Eulerian-Lagrangian technique

In this research, the XCC pile installation and soil consolidation processes were modelled using an in-house developed effective-stress large deformation finite element approach, i.e., dual-stage Eulerian-Lagrangian (DSEL) technique. Since the development of DSEL has been reported in detail by Yi *et al.* (2012, 2014), only a brief description with bare essentials is presented herein. The DSEL approach is comprised of three integrated modules namely the effective-stress Eulerian module, the coupled-flow Lagrangian module, the mesh-to-mesh variable mapping module. The effective-stress Eulerian module is developed to model the rapid foundation installation which features large deformation and strain without obvious dissipation of excess pore pressure (i.e., undrained conditions), while the coupled-flow Lagrangian module is suitable for analyzing the post-installation consolidation response, which is characterised by a limited quantity of deformation and yet apparent pore pressure dissipation. The mesh-to-mesh variable mapping module acts as bridge between these two modules, which transfers the simulated results from the end of the one module to the beginning of the other. Briefly, simulating the installation and consolidation of the foundation were completed in two separate stages, and the solution mapping was conducted outside the ABAQUS environment.

2.2 Validation of the DSEL technique

Although several validation cases have been reported in Yi *et al.* (2012, 2014), the robustness and reliability of the DSEL technique were verified to model offshore spudcan foundations, rather than jacked piles. To verify the latter, DSEL approach is used in this section to replicate centrifuge test of jacked piles and the field installation test of XCC piles reported in the literature.

2.2.1 Comparison with the centrifuge test reported in Li et al (2017) and Li et al. (2017a)

Table 1 Properties of the Shanghai soft soil

Effective unit weight (γ')	8.75 kN/m^3
Effective internal friction angle (φ')	30°
Slope of isotropic virgin compression line (λ)	0.11
Slope of swelling/recompression line (κ)	0.02
Coefficient of earth pressure at test (K_0)	0.55
Overconsolidation ratio (OCR)	1.0
Coefficient of permeability (k)	2.67×10^{-9} m/s
Initial void ratio (e_0)	0.98

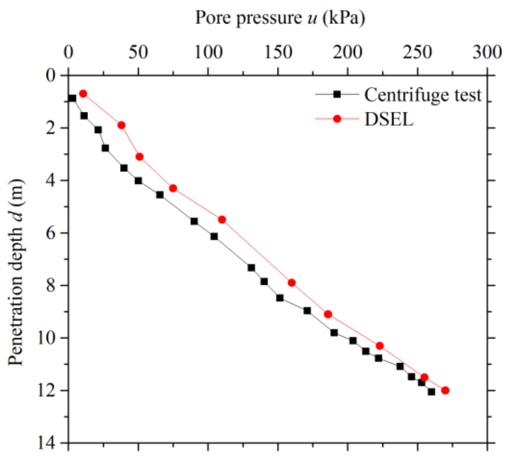

Fig. 3 Variation of pore pressure with pile penetration depth at the pile shoulder position

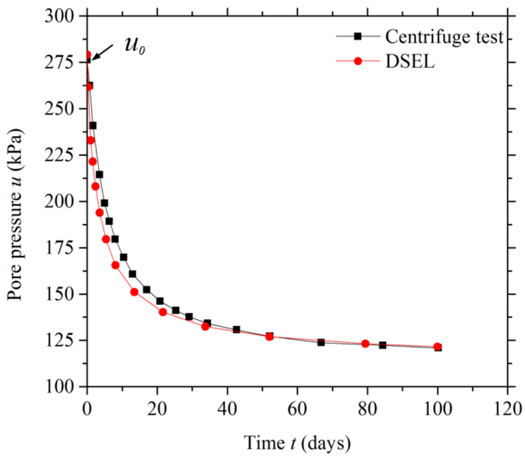

Fig. 4 Dissipation of pore pressure after pile installation at the pile shoulder position

Li *et al* (2017) and Li *et al*. (2017a) published a serial of centrifuge test data, including single pile installation and consolidation at the 50 g model gravity. The normally consolidated (NC) soil was prepared by remoulding and reconsolidating soil taken from the fifth geological stratum in Shanghai city, and the soil properties are summarized in Table 1. When centrifuge was spinning, a 10 mm-diameter model pile fitted with a 60° conical tip was jacked at a constant rate of 50mm/min into the soil until reaching a depth of 250 mm. This relatively fast penetration rate was adopted to ensure fully undrained condition during pile

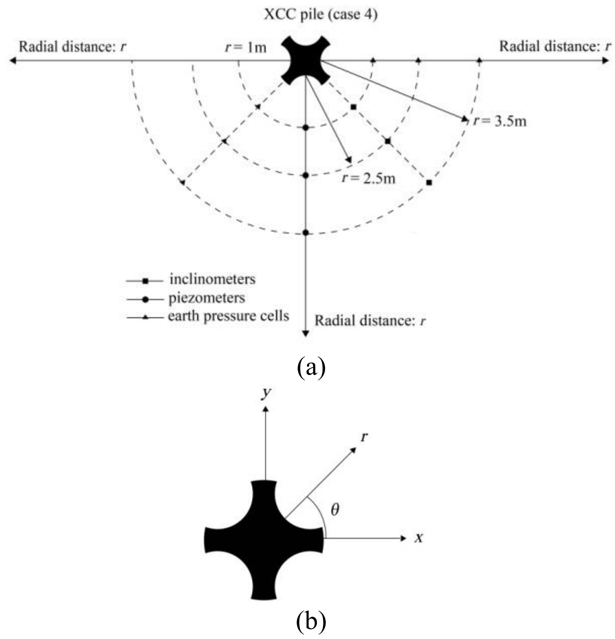

Fig. 5 XCC pile field test: (a) plan view of various sensors and (b) polar angle in cylindrical coordinate system (Zhou *et al*. 2018).

installation. In an attempt to record the excess pore pressure variation during the pile installation and subsequent soil consolidation, a mini pore pressure transducer was inserted 10 mm above the pile tip (i.e., at the pile shoulder level). The constitutive behaviour of soil was modelled with the modified Cam-clay (MCC) model using the material parameters summarized in Table 1. According to Mahmoodzadeh *et al.* (2015), the MCC model is recognised to be more appropriate to capture the mechanical behaviour of normally or lightly over-consolidated clays. The details of the established numerical model and the boundary conditions are similar to the analysis of XCC pile described in Section 2.3, which will be described in detail later on. Only the computed results are presented and discussed herein.

The calculated and experimentally measured pore pressure (u) results at the pile shoulder are compared in Fig. 3. For the sake of clarity, the test results are described as prototype scales hereinafter unless otherwise stated. The numerical calculated results (labelled "DSEL" in the graph) in Fig. 3, which are in good agreement with that from the centrifuge test, indicating that the pore pressure increases approximately linearly with penetration depth. Such a trend has also been observed in some field tests, which attributes to the linear strength profile of the NC clay layers. Fig. 4 compares the numerically calculated pore pressure dissipation curve and the centrifuge test results at the same position. The calculated dissipation results are read from Lagrangian stage of DSEL analysis. Its initial pore pressure value (labelled "u_0" in Fig. 4) coincides with the u calculated at the final depth of Fig. 3, as a result of solution mapping explained earlier. Overall, a satisfactory agreement is achieved between the measured and calculated results, which validates the reliability of the DSEL technique in modelling long-term soil responses.

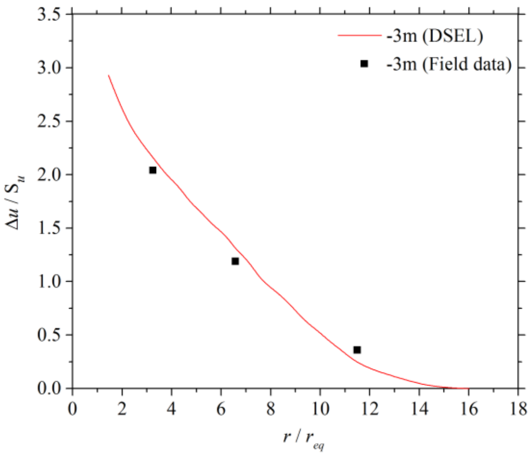

Fig. 6 Variation of normalized excess pore pressure with normalized radial distance ($\theta = 45°$)

2.2.2 Comparison with the field test reported in Zhou et al. (2018)

A series of field tests of XCC piles were conducted in deltaic deposits, located near the 4th Yangtze River Bridge in Nanjing. The excess pore pressure and soil displacement induced by XCC pile installation were measured during the field tests. As shown in Fig. 5(a), various sensors to measure excess pore pressure, soil displacement were used at two clusters (at depths of 3 m and 6 m) located along the $\theta = 0°$ and $\theta = 45°$ polar directions (the θ is the angle between the vertical profile r and the vertical profile x as shown in Fig .5(b)), and the radial distance is equal to 1 m, 2 m and 3.5 m, respectively. The experimental site mainly consists of soft silty clay and medium silty clay. The soil strength in the soft and medium stiff clays is approximately 10 kPa and 25 kPa respectively according to the CPT results. Further details concerning the measurement of the test piles can be found in Zhou *et al*. (2018).

Fig. 6 compares the excess pore pressure variations calculated from the DSEL technique and measured from the field test. In the figure, the excess pore pressure Δu is normalized by the corresponding in-situ soil strength s_u and the radial distance r from the XCC pile axis is normalized by the equivalent radius r_{eq}. As shown in Fig. 6, Δu / s_u presently calculated was proved to be in reasonable agreement with that reported in the literature. This further enhances the credibility of the DSEL analysis results.

2.3 Finite element models

Fig. 7(a) shows the Eulerian finite element model established for the first stage, which simulates the large deformation, undrained continuous installation of the pile. Owing to the symmetry, only a quarter of the geometrical model was adopted. Note that the numerical model XCC pile is identical to the circular pile except for the pile geometry. The cross-sectional geometry parameters of the XCC pile are $\alpha = 0.82$ m, $b = 0.18$ m and $\theta_0 = 130°$, and the cross-sectional area and perimeter are $A_x = 0.28$ m^2 and P_x = 2.85 m respectively. The diameter of the circular pile is 0.6 m, with a cross-sectional area of $A_c = 0.28$ m^2 and a cross-sectional perimeter of $P_c = 1.88$ m, the two model piles thus have the same cross-section area. Since the emphasis of this study is the responses of soil, the pile deformation was not considered and it was modelled as a rigid Lagrangian body with infinite stiffness.

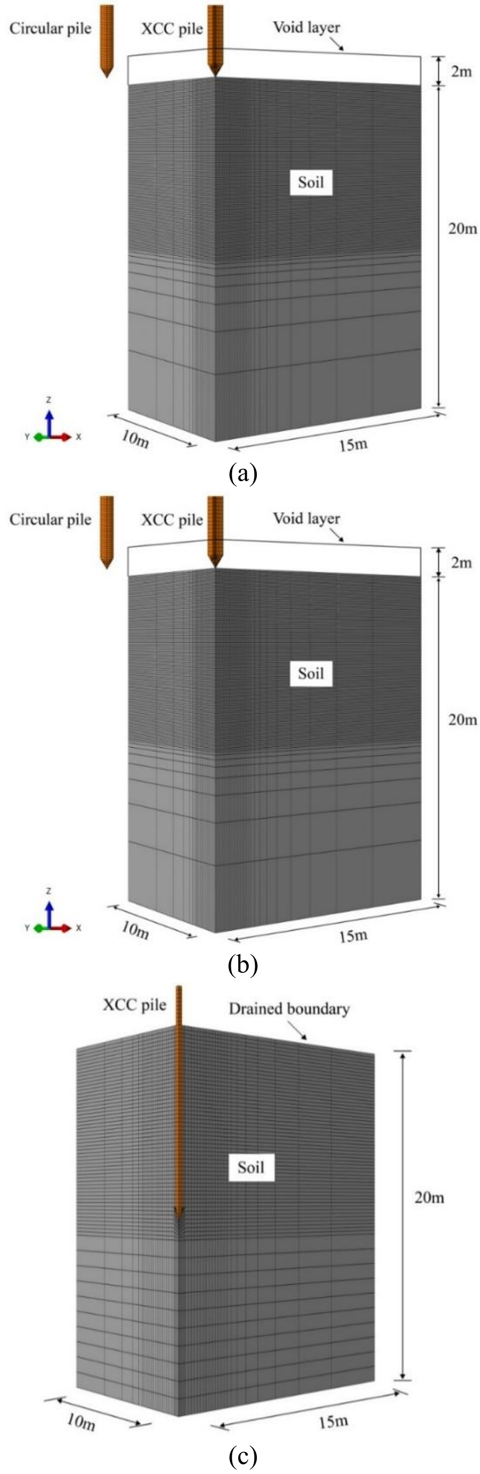

Fig. 7 Finite element model: (a) Eulerian finite element model (undeformed), (b) Eulerian finite element model (deformed) and (c) Lagrangia finite element model

Right underneath the pile tip lies a cuboidal soil model, 20 m in height by 15 m in width by 10 m in thickness. During the pile installation process, in order to accommodate the anticipated large deformation, the soil body was modelled as Eulerian domain and discretized into 8-noded Eulerian brick elements. The graded Eulerian mesh was adopted to balance the computational effort and accuracy, as shown in Fig. 7(a), the finer meshes were prescribed in the inner part, while coarser meshes were prescribed in the outer portion. A layer of 2-meter-thick of voids, without strength and stiffness, is located on the top of the soil domain. This was to cater for soil heave and move above the initial soil surface during the pile installation. During analysis, soil flows normal to the side and bottom surfaces of the cuboid were constrained against the flow in the vertical direction, while tangential components were allowed.

The constitutive behaviour of soil was modelled by the modified Cam-clay (MCC) model with parameters listed in Table 1. The interface between pile and soil was commonly applied using a general contact form which can allow arbitrary sliding at pile-soil interaction. Pile-soil friction was defined as fully smooth for simplicity. The initial stress distribution of Stage 1 was specified to follow the K_0 stress condition before the pile installation, and remains constant throughout the analysis. During the calculation, a constant prescribed rate of 0.1 m/s was imposed at the pile to model continually installation of the pile into soil domain until reaching a depth of 10 m. Since the Eulerian calculation is essentially an undrained analysis, such this selected rate is irrelevant as long as it is not too fast to bring in dynamic effect.

Upon the completion of the first stage, the deformation geometry of soil was extracted from Eulerian model (see Fig. 7(b)), which was then used to establish the Lagrangian model (see Fig. 7(c)) for the second (Lagrangian) stage. (Note that the insignificant soil heave induced by the pile installation in the former stage was not reflected in the latter stage to facilitate the establishment of the model). In other words, the initial geometry of the Lagrangian model was equivalent to the deformation of the Eulerian domain, but their mesh layouts can be different. Various solution variables (including various stress components, void ratio, pore pressure) were then transferred from the Eulerian analysis to Lagrangian analysis through the mesh-to-mesh mapping module. Thereafter, drainage only was allowed at the top of the soil domain, and the couple-flow analysis was performed to model the soil consolidation responses.

3. Result and discussion

This section presents the calculated results and relevant discussions about XCC pile analysis. Before moving to the details, it may be more convenient to provide an overview. This section roughly consists of two parts, the first part mainly clarifies the difference in radial total stress as well as excess pore pressure during the installation of XCC pile and circular pile. The emphasis of the second part on research is on the time-dependent soil strength variations and the set-up effects on XCC pile shaft resistance.

3.1 Radial total stress and pore pressure variation during the installation stage

3.1.1 Total radial stress variation

During XCC pile and circular pile installation, the peak

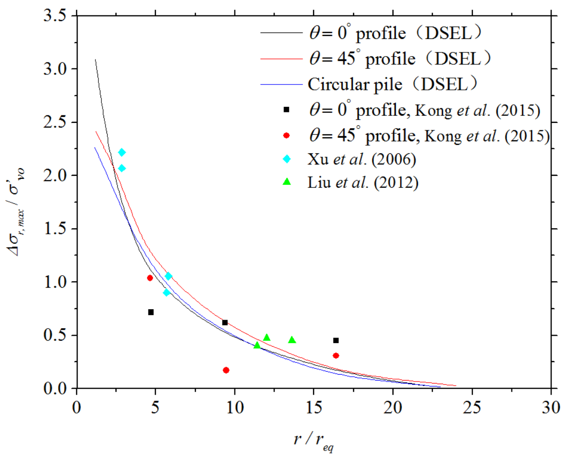

Fig. 8 Normalized maximum variation of the radial total stress along the radial distance

variations in radial total stress along the lateral distance are shown in Fig. 8. To compare directly and conveniently with other historical field test results obtained at different sites, a normalized parameter can be used to describe the development of radial total stress induced by the pile installation, namely the $\Delta\sigma_{r,max}$ / σ_{vo} ratios, $\Delta\sigma_{r,max}$ herein denotes the maximum value of radial total stress increase during pile installation process, and σ'_{vo} is the corresponding in-situ vertical effective stress. These simulation results are compared with the data of $\Delta\sigma_{r,max}$ / σ_{vo} published by Kong *et al.* (2015) during the installation of an XCC pile in soft clay, and those published by Xu *et al.* (2006) and Liu *et al.* (2012) during the installation of an open-ended pile in soft clay. Although some data points are somewhat scattered due to the difference in soil properties, pile types or installation methods, most of the data points are broadly close to the calculation results of the two numerical piles. Besides, both computed results of the two kinds of piles show a nearly logarithmic decrease of the $\Delta\sigma_{r,max}$ / σ_{vo} ratio with the distance to the pile axis beyond about $5r_{eq}$, while the decrease is very steep close to the pile. Furthermore, for XCC pile, the computed $\Delta\sigma_{r,max}$ value in θ = 0° and θ = 45° vertical profile near XCC pile shaft interface would be about $3.15\sigma'_{vo}$ and $2.4\sigma'_{vo}$, respectively. Those computed results indicate that the radial stress distribution of XCC pile is non-axisymmetric, for another, it also illustrates the larger soil densification development near the pile shaft at θ = 0° radial profile during XCC pile installation.

3.1.2 Excess pore pressure generation

Figs. 9(a) and 9(b) and Fig. 9(c) present the contours of excess pore pressure (Δu) developed at the end of driving (EOD) of XCC pile and circular pile respectively, based on calculation results of the first stage (Eulerain) analysis. Two radial profile (θ = 0° and θ = 45°) of the XCC pile and a vertical profile of circular pile are selected for comparative analysis. It can be seen obviously from the Figs. 9(a) and 9(b) and Fig. 9(c) that, for XCC pile and circular pile, the high Δu occurs in the soil zones close to pile shaft and pile tip. Such high Δu in this zones is the result of the strong

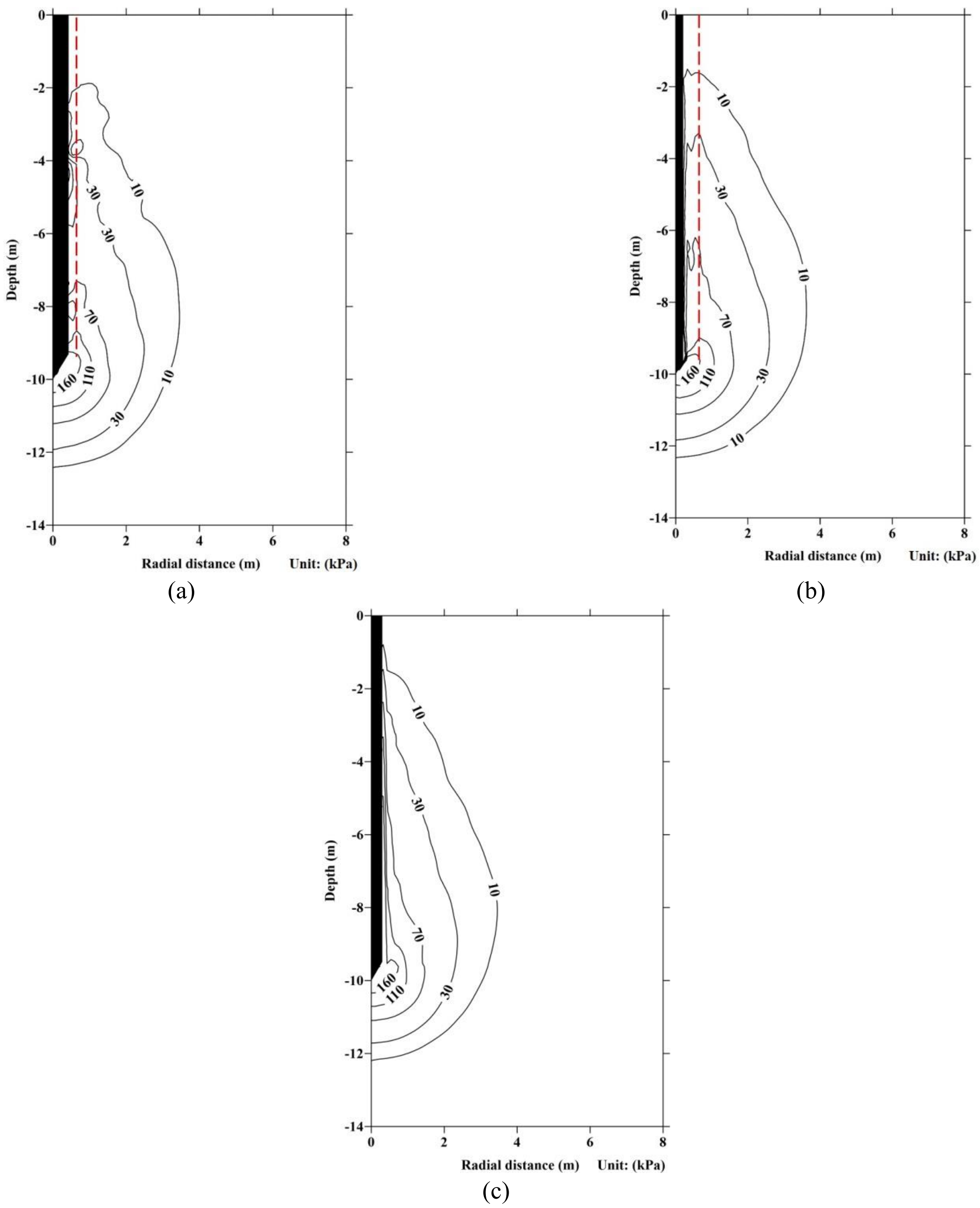

Fig.9 The excess pore pressure contours after pile installation: (a) θ = 0° profile for XCC pile, (b) θ = 45° profile for XCC pile and (c) circular pile

extrusion, large deformation and strain effects (Lee *et al*. 2009, Silvestri *et al*. 2012, N*i et al.* 2017, Li *et al*. 2020). In term of the shape of the contour of Δu, both of the two piles in simulation show the approximate tear shape, and the build-up of Δu value and scope located beneath the pile as well as surrounding the conical shoulder is almost equal. However, for the soil zone near the pile shaft, there are significant differences in the calculated Δu between XCC pile and circular pile. As shown in Figs. 9(a) and 9(b), the calculated Δu near XCC pile shaft is lower than that close to circular pile shaft, and the peak value of the Δu induced by XCC pile installation is not located at the pile-soil surface, but at a very short distance from the pile wall (labeled by red imaginary line). This distribution trend is distinctly different from that of the circular pile, in the latter, the peak value of the Δu exists at the pile-soil interface. This being may be attributed to the XCC pile penetration–induced shear dilatation effect in this soil zones near the XCC pile shaft. It is generally believed that, during pile penetration process, the variation in Δu mainly raises from two sources: (1) the change of mean stress which results from outward expansion of the soil by the installing pile and (2) the change of shear stress, which is caused by the shear deformation of the soil near the pile wall (Kim *et al*. 2007, Li *et al*. 2016, N*i et al.* 2018). Different from the soil zones below the pile tip, the shear stress become a major component of the induced Δu along the surface of the pile body (Burns *et al*. 1998). The shear stress induced by the

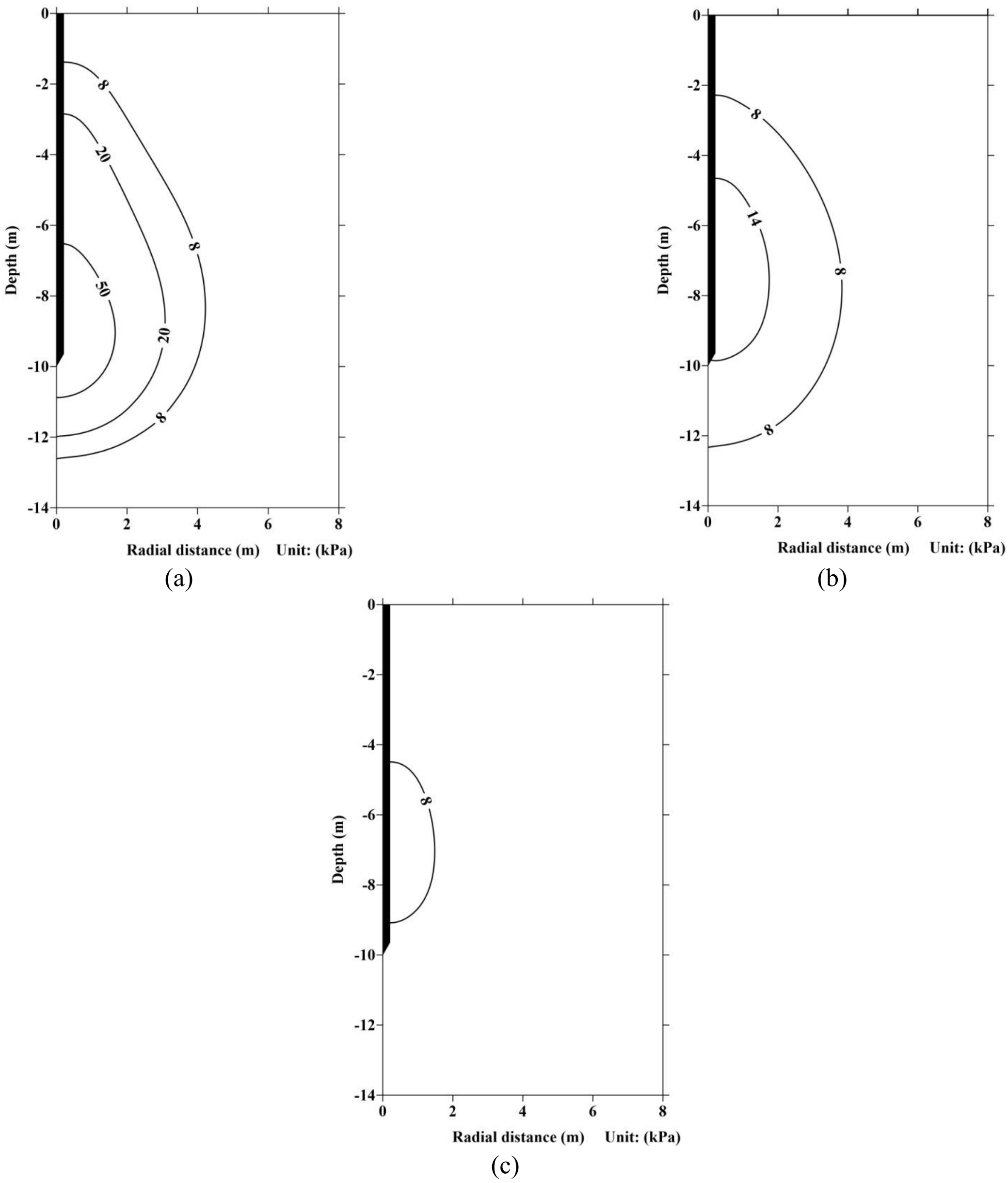

Fig. 10 The excess pore pressure contours computed along $\theta = 45°$ profiles at (a) 3 days, (b) 30 days and (c) 60 days after EOD XCC pile

XCC pile penetration is large near the pile-soil interface due to the effect of the X-shaped cross-section, as a result, the soil dilatancy may be generated. Since the shearing effect related with pile penetration is an undrained process in clay, thus the dilatancy effect of the soil elements adjacent to pile-soil interface will give rise to a reduction in Δu due to the generation of negative excess pore pressure (Basu *et al*. 2014). Another possible reason may be the partial unloading effect in that some soil elements move from the XCC pile surface to the tip of pile in vertical direction during installation process, which makes these soil elements tend to be tensile, thus the value of the Δu near the pile surface is reduced by this partial unloading effect (Chai *et al*. 2016).

Figs. 9(a) and 9(b), it is also seen that the distribution of the Δu along the $\theta = 0°$ and $\theta = 45°$ radial profile of XCC pile is generally similar, but there are still some discrepancies between the two vertical profiles. For $\theta = 0°$ radial profile, the peak value of Δu is located at a distance of about $1.3r_{eq}$ from the pile-soil interface, while for $\theta = 45°$ radial profile, it is reached at a radial distance about $2.5r_{eq}$ from the pile-soil interface. Kim *et al* (2007) linked these features with shear zone radius that defined as the interface between the shear and plastic zones where the peak value of Δu is caused. Therefore, for $\theta = 0°$ and $\theta = 45°$ radial profile, the influence range of the shear stress induced by the XCC pile installation is 1.3 r_{eq} and 2.5 r_{eq}, respectively. These results also indicate that the penetration–induced shear stress zone range along the $\theta = 0°$ profile is lower than that of the $\theta = 45°$ radial profile.

3.1.3 Consolidation after pile installation

Figs. 10(a)-10(c) show the gradual Δu dissipation along the $\theta = 45°$ vertical profile after EOD XCC pile, which are plotted based on computed results of the second

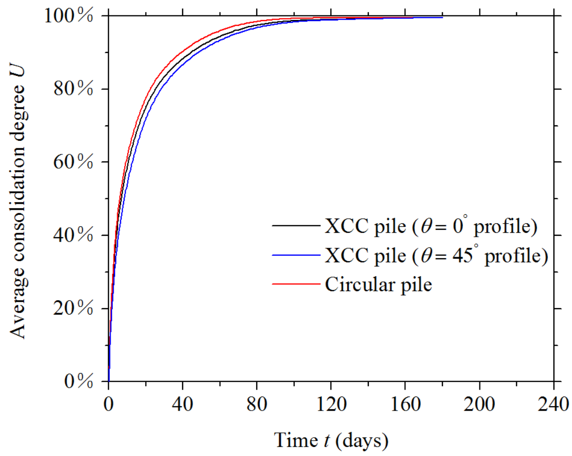

Fig. 11 Development of consolidation degree U with time after EOD XCC pile and circular pile

(Lagrangian) stage. By the comparison of Fig. 9(a) and Fig. 10(a), it can be seen that the influenced area of Δu (i.e., the area with Δu > 8kPa) shrink slightly 3 days after EOD XCC pile, while the value of Δu reduce substantially. Subsequently, as shown in Fig. 10, the magnitude of Δu influence zone and the value of Δu decrease gradually with consolidation. In Fig. 10(c), it is clear that most of the Δu dissipated within about 60 days after EOD XCC pile. Fig. 11 shows the entire time history of the consolidation process, where U is the average consolidation degree along the whole radial profile according to Eq. (1).

$$U = 1 - \frac{\iint_A \Delta u da}{\iint_A \Delta u_{EOD} da} \tag{1}$$

where Δu_{EOD} denotes Δu at EOD Pile i.e., those in Fig. 9 and A is the area of the radial profile. As the graph shows, for the two numerical piles, the time for the fully dissipation of Δu is approximately 120 days. However, there are some slight differences between XCC pile and circular pile with regard to the dissipation rate of Δu. In Fig. 11, it can be found that, for these two vertical profiles of XCC pile, the Δu dissipation rate is slightly slower compared with the circular pile. This phenomenon is mainly because the large positive value of Δu lies a few distances away from the XCC pile wall, at the early stages of consolidation, the pore water flows initially toward the XCC pile wall because of the redistribution of Δu. Thereafter, like the circular pile, the traditional pattern of radial pore water flowing away from the XCC pile wall is established, adding to the time for the decay of Δu and thus decrease the dissipation rate of Δu.

3.2 Enhancement of soil strength

This section presents the effect of Δu dissipation on soil strength conditions after completing XCC pile installation. Particular attention is focused on evaluating soil strength enhancement during consolidation with respect to in-situ strength state, and the quantum of strength enhancement is built. The difference in strength improvement near the

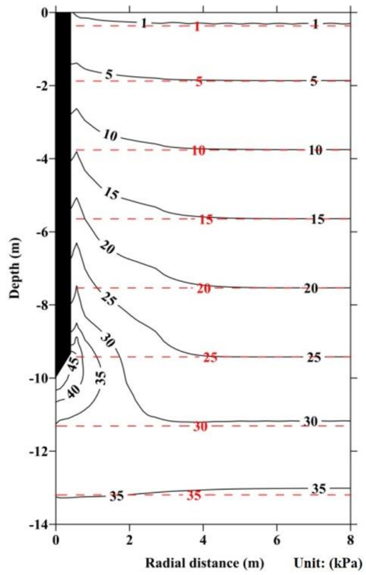

(a)

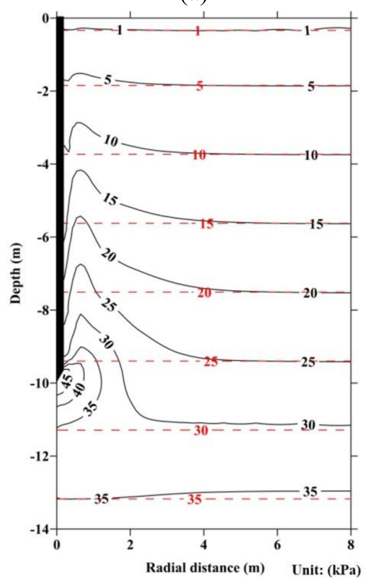

(b)

Fig. 12 Contour of soil's undrained shear strength s_u around XCC pile at U = 100%: (a) θ = 0° profile and (b) θ = 45° profile

concave side and flat side of XCC pile is analyzed, and the role of Δu dissipation on set-up is quantitatively assessed in terms of the XCC pile shaft resistance.

3.2.1 Variations of soil strength during consolidation

Figs. 12(a) and 12(b) show the contours of soil undrained shear strength (s_u) in the two vertical profiles of XCC pile at the end of consolidation (EOC), which is compared with the in-situ strength (s_{u0}) (labelled by red dashed line). Noted that s_u was herein deduced from Lagrangian calculation results of mean effective normal stress p' and isotropic over-consolidation ratio R_i by Wroth's relationship

$$s_u = \frac{M}{2} p' \left(\frac{R_i}{2}\right)^{\frac{\lambda-\kappa}{\kappa}} \tag{2}$$

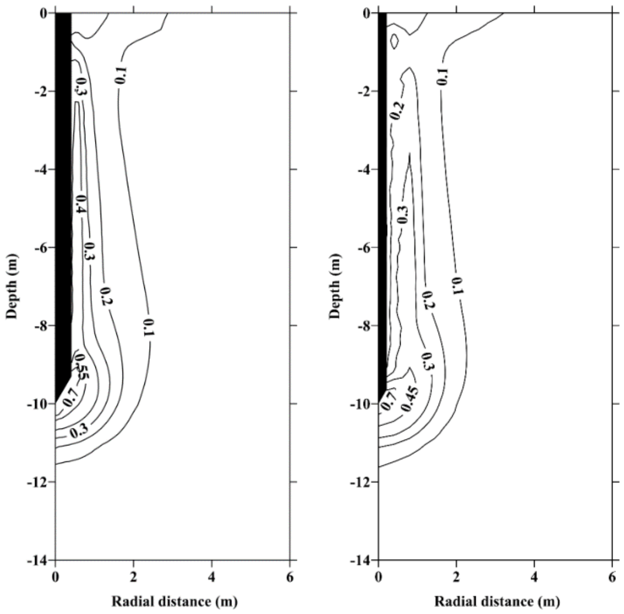

(a) (b)

Fig. 13 Contour of soil strength improvement ratio R_s around XCC pile at U = 100%: (a) θ = 0° and (b) θ = 45°

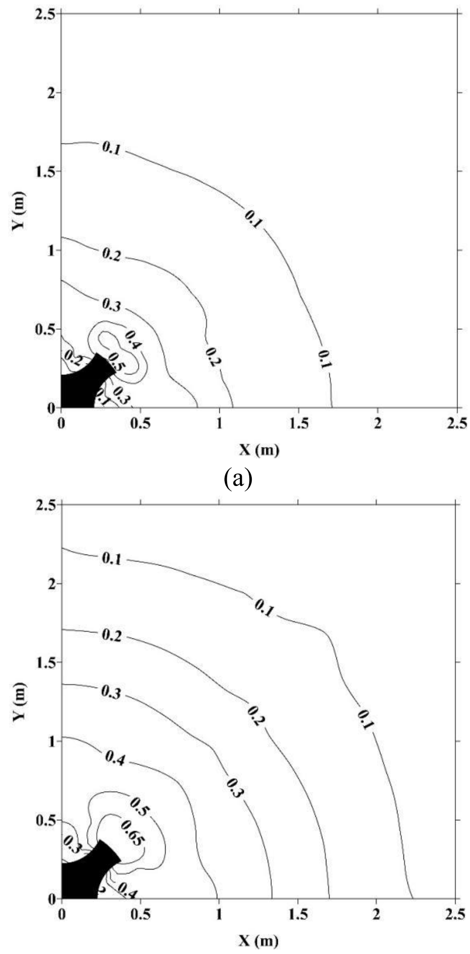

(a)

(b)

Fig. 14 Contour of soil strength improvement ratio R_s around XCC pile at U = 100%: (a) 5 m depth and (b) 9 m depth

where M is gradient of the critical state line; λ is the slope of the isotropic virgin consolidation line, κ is the slope of swelling or recompression line. After consolidation, significant strength increment can be observed around XCC pile, this enhancement is more noticeable near the pile tip and shoulder, where the s_u increases from about 25 to 45kPa. However, in the 45° vertical profile, the s_u next to the pile shaft is slightly lower than that of the 0° vertical profile, and this phenomenon can be explained by the fact that soils falling in the installation path of the pile have been dragged down to greater depths by the continuous pile installation.

From a practical viewpoint, the long-term strength after pile installation may be more meaningful. The long-term strength improvement of soils at the EOC XCC pile is shown in Figs. 13(a) and 13(b). The enhancement of soil strength herein is quantified by the soil strength improvement ratio R_s, which is defined as the percentage of strength improvement with respect to the in-situ soil strength i.e., $R_s = \frac{s_u}{s_{u0}}$ -1. Obviously, these graphs vividly present the range and magnitude of soil strength improvement around XCC pile after full consolidation. Assuming that R_s > 0.1 is the outer boundary of the soil strength improvement area, Figs. 13(a) and 13(b) present that the area with strength improvement extends horizontally by approximately 8 times r_{eq} from the XCC pile axis and vertically by the 1.5m below the XCC pile tip.

Figs. 14(a) and 14(b) plot the soil strength improvement ratio distribution around the XCC shaft in the horizontal section at the depths of 5 m, 9 m, respectively. It can be found that the contours of R_s exhibit a non-circular distribution characteristic near the XCC pile shaft because of the X-shaped cross-section effects, and this non-circular distribution of the contours gradually disappears with the increase of radial distance to the XCC pile shaft center until the contours of R_s turn into circular curves. This indicates that the shape of XCC pile cross section only influences the soil deformation close to the pile shaft, while this shape influence disappears far away from the pile shaft. In addition, in Figs. 14(a) and 14(b), it is also seen that the R_s near the flat side is distinctly larger than that near the concave side at the depths of 5 m and 9 m. For example, in horizontal section at the depth of 5 m, the R_s near the flat side can reach approximately 0.5, while the calculated R_s close to the concave side only can attain 0.1-0.3. This phenomenon can be directly attributed to two parts: On the one hand, the more intensive soil densification effect occurs adjacent to the flat side during the XCC pile installation, which leads to the higher mean effective stress and thus the more strength improvement takes place. On the other hand, for soil adjacent to concave side, as discussed earlier, the soil near the concave side is dragged down to greater depths because of the concave shape effect during the XCC pile installation, thus the relatively less soil strength improvement develops.

As shown above, the soil strength which is below XCC pile tips and near the pile shaft, increases significantly, and for XCC pile shaft, the soil strength enhancement degree near the flat side is greater than that near the concave side. The next section will evaluate and quantify the set-up effects on XCC pile shaft resistance.

3.2.2 Set-up effects on XCC pile shaft friction

In pile foundation design, the α (total stress) approach is still a widely used method to calculate the average pile shaft capacity in cohesive soils.

$$f_{s,ave} = as_u \tag{3}$$

where α is a dimensionless factor. Therefore, the reliable prediction of f_s is largely dependent on confirming the value of α and s_u. With regard to the α value, much of research work has been reported in the literature, with many findings having been incorporated into the current design guidelines such as API 2002. However, for the s_u value, it is common to neglect set-up effects and take it as in-situ strength before the pile installation i.e., $s_u = s_{u0}$. This is largely due to the lack of understanding the updated soil strength or strength enhancement during the pile installation and soil consolidation.

As previously mentioned, the R_s can be used to quantify the soil strength improvement. To link the set-up effect to the shaft resistance, the updated expression incorporated set-up effects as follows:

$$f_{s,ave} = as_{u0}(1+R_s) \tag{4}$$

From a practical perspective, an average value along the whole XCC pile shaft wall $R_{s,ave}$ is more significant for utilization with Eq. (4). As can be observed from the Figs. 13(a) and 13(b), in the θ = 0° and θ = 45° vertical profile, the variations of R_s along the XCC pile shaft are insignificant, thus the $R_{s,ave}$ can be obtained by calculating the surface integral R_s with respect to the XCC pile shafts surfaces S, as follows:

$$R_{s,ave} = \frac{1}{S}\iint_S R_s ds \tag{5}$$

Based on the calculation results of the second stage, the $R_{s,ave}$ over the flat side and concave side can be respectively calculated by the integration of the R_s in the flat side and concave side. The whole time history of computed $R_{s,ave}$ was obtained and presented in Fig 15. It can be clearly seen that the $R_{s,ave}$ of the flat side and concave side increase substantially with time, while the increase in magnitude and the increase in rate decrease with time during the consolidation process, and gradually increase toward a final equilibrium value $R_{s,ave}^{t\approx\infty}$ after about 120 days. Although, the time-dependent variable trend of $R_{s,ave}$ in flat side and concave side is almost the same, the $R_{s,ave}^{t\approx\infty}$ of the flat side is almost 2.5 times that of concave side because the more R_s is generated in the flat side. Fig. 16 also demonstrates the whole time history of $R_{s,ave}$ in the circular pile. Comparing the computed results of XCC pile and circular pile, it appears that the $R_{s,ave}$ value of circular pile at any moment is greater than that of concave side in XCC pile, but less than that of flat side in XCC pile.

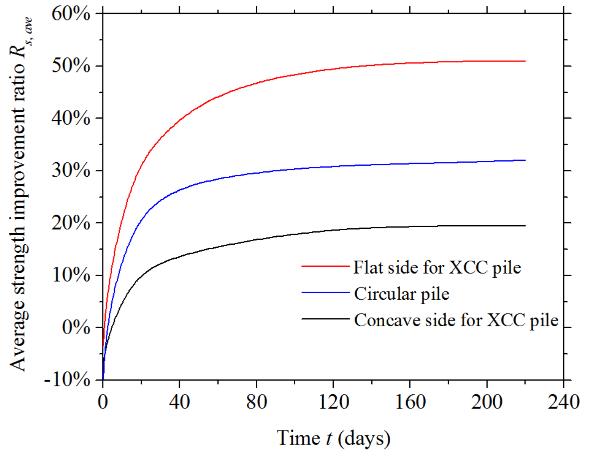

Fig. 15 Development of average strength improvement ratio $R_{s,ave}$ with time over the pile shaft surface

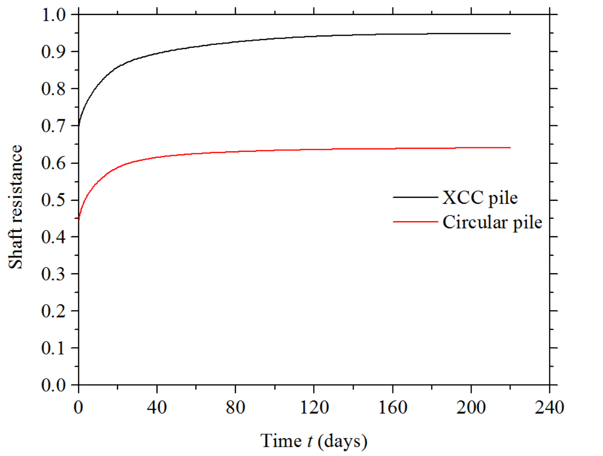

Fig. 16 Development of pile shaft resistance with time

Besides, it can also be seen from Fig. 16 that the $R_{s,ave}$ value of the circular pile increases fast compared with the two sides of the XCC pile. This is due to the quicker Δu dissipation rate of the circular pile as discussed in Section 3.1.3.

The ultimate pile shaft resistance f_s can be calculated by the following equation:

$$f_{s,ave} = as_{u0}C(1+R_{s,ave}) \tag{6}$$

where C donates the cross-sectional perimeter of the pile. For XCC pile, the shaft resistance is composed of two parts, concave side resistance and flat side resistance, which are equal to the arc length multiply by the corresponding $f_{s,ave}$. Since the identical soil parameters are used in modelling XCC pile and circular pile, Fig. 16 only shows the calculated results of $C(1+R_{s,ave})$ evolution with consolidation time, and this treatment does not influence the comparison of the circular pile and XCC pile with respect to shaft resistance. It is clear that the f_s displays an increase trend with the passage of time, the final equilibrium value $f_s^{t\approx\infty}$ of XCC pile and circular pile are about 0.94 and 0.65, respectively. Considering the fact that, with the identical cross-sectional area of the two numerical piles, the perimeters of XCC pile are approximately 52% higher than that of the circular pile (2.85m versus 1.88m), Theoretically, the $f_s^{t\approx\infty}$ of XCC pile should also be 52% larger than that of the circular pile. However, the calculated $f_s^{t\approx\infty}$ of XCC pile is approximately 1.45 times that of the circular pile (0.94 versus 0.65), the main reason for this discrepancy is that the installation-induced excess pore pressure accumulation around the XCC pile shaft is slightly lower than circular pile, and the soil strength improvement mainly derives from the dissipation of excess pore pressure (Li *et al* .(2016), Wang *et al*. (2019)), therefore the soil strength improvement near the XCC pile shaft is smaller than that of circular pile shaft. This explains why the $f_s^{t\approx\infty}$ increment of the XCC pile is less than 52% compared with the circular pile.

4. Discussion

To date, most analyses on XCC pile performance commonly ignore the pile installation and soil consolidation process, which brings lots of uncertainty for the design of XCC pile to be used in practice. Thus this study reveals the pile installation and soil consolidation mechanism of XCC pile using an in-housed developed DSEL technique, especially the time-dependent strength property close to pile shaft, which has a crucial role in XCC pile shaft resistance incorporated the set-up effects. The findings from this study may be beneficial for facilitating the incorporation of set-up effects into XCC pile design practices. Although the loading of XCC pile is not modelled in this study, the calculated results based on DSEL computed technique are able to capture principal traits of set-up effects as regards the XCC pile shaft resistance scientifically and rationally. To refine the analysis shown herein, more vigorously investigations, for instance, the analysis of the time-dependent bearing capacity of XCC pile during pile loading stage, a parametric study of the effect X-shaped cross-sectional geometry on the set-up phenomenon, would make the research of XCC pile set-up phenomenon more accurate and abundant. However, this is beyond the scope of this paper.

5. Conclusions

In this study, the DSEL calculation technique was carried out to continually model the jacking installation and consolidation of XCC pile. The calculation results were verified by comparison with previous centrifuge tests and field tests. The installation mechanism as well as time-dependent soil behavior around the XCC pile shaft are extensively investigated. The primary conclusions can be summarized as follows:

• maximum increment in radial total stress near the XCC pile shaft shows a logarithmic decreasing trend with radial distance, and the soil densification effect near the pile shaft at θ = 0° radial profile is larger than that at θ = 45° radial profile.

• the high excess pore pressure of XCC penetration-induced is not located on pile-soil interface, but exists a very short radial distance from the pile shaft. The shear stress zone range near the pile shaft in θ = 45° radial profile is higher than that in θ = 0° radial profile.

• the excess pore pressure dissipation rate of circular pile is sightly quicker than that of XCC pile.

• the zones of discernable soil strength improvement as well as improvement magnitude are established. Soil near the flat side and concave side of XCC pile shaft arrive strength increase of different quantity, with more strength development occurring adjacent to flat side.

• the effect of consolidation on soil strength improvement and the set-up influence on the XCC pile shaft resistance are quantified. Computed results indicate that the consolidation influence on soil strength improvement close to the flat side and concave side is significant, while the final $R_{s,ave}^{t\approx\infty}$ near the flat side is greater than that in the concave side. In addition, the calculated ultimate shaft resistance of XCC pile incorporated into set-up effects is approximately 45％ higher than that of circular the pile.

Acknowledgments

The authors wish to express their thanks to the very competent reviewers for the valuable comments and suggestions. The research described in this paper was financially supported by the Natural Science Foundation of China (Grant/Award Numbers: 51778091), the graduate scientific research and innovation foundation of Chongqing, China (Grant/Award Numbers: CYS18023).

References

API (2002), *Recommended Practice for Planning, Designing and Constructing Fixed Offshore Platforms-Working Stress Design*, American Petroleum Institute, Washington, U.S.A.

Azari, B., Fatahi, B. and Khabbaz, H. (2015), "Numerical analysis of vertical drains accelerated consolidation considering combined soil disturbance and visco-plastic behaviour", *Geomech*. *Eng*., **8**(2), 187-220. https://doi.org/10.12989/gae.2015.8.2.187.

Basu, P., Prezzi, M., Salgado, R. and Chakraborty, T. (2014), "Shaft resistance and setup factors for piles jacked in clay", *J. Geotech*. *Geoenviron*. *Eng*., **140**(3), 04013026. https://doi.org/10.1061/(ASCE)GT.19435606.0001018.

Burns, S. and Mayne, P. (1998), "Monotonic and dilatory pore-pressure decay during piezocone tests in clay", *Can*. *Geotech*. *J*., **35**(6), 1063-1073. https://doi.org/10.1139/cgj-35-6-1063.

Ceccato, F., Beuth, L., Vermeer, P.A. and Simonini, P. (2016), "Two-phase material point method applied to the study of cone penetration", *Comput*. *Geotech*., **80**, 440-452. https://doi.org/10.1016/j.compgeo.2016.03.003.

Chai, J.C., Hossain, M.J., Yuan, D.J., Shen, S.L. and Carter, J.P. (2016), "Pore pressures induced by piezocone penetration", *Can*. *Geotech*. *J*., **53**(3), 540-550. https://doi.org/10.1139/cgj-2015-0206.

Ding, X.M., Luan, L.B., Liu, H.L., Zheng, C.J., Zhou, H. and Qin, H.Y. (2020), "Performance of X-section cast-in-place concrete piles for highway constructions over soft clays", *Transport*. *Geotech*., **22**, 100310. https://doi.org/10.1016/j.trgeo.2019.100310.

Hamann, T., Qiu, G. and Grabe, J. (2015), "Application of a Coupled Eulerian-Lagrangian approach on pile installation problems under partially drained conditions", *Comput*.

Geotech., **63**, 279-290. https://doi.org/ 10.1016/j.compgeo.2014.10.006.

Kim, T., Kim, N, K., Tumay, M.T. and Lee, W. (2007), "Spatial distribution of excess pore-water pressure due to piezocone penetration in overconsolidated clay", *J. Geotech. Geoenviron. Eng*., **133**(6), 674-683. https://doi.org/10.1061/(ASCE)10900241(2007)133:6(674).

Kong, G.Q., Zhou, H., Ding, X.M. and Cao, Z.H. (2015), "Measuring effects of X-section pile installation in soft clay", *Proc. Inst. Civ. Eng. Geotech. Eng*., **168**(4), 296-305. https://doi.org/10.1680/geng.14.00048.

Lee, J., Kim, M. and Lee, S. (2009), "Reliability analysis and evaluation of LRFD resistance factors for CPT-based design of driven piles", *Geomech. Eng*., **1**(1), 17-34. https://doi.org/10.12989/gae.2009.1.1.017.

Li, C., Zou, J.F. and Li, L. (2020), "A novel approach for predicting lateral displacement caused by pile installation", *Geomech. Eng*., **20**(2), 147-154. https://doi.org/10.12989/gae.2020.20.2.147.

Li, J.P., Li, L., Sun, D.A. and Gong, W.B. (2017), "Time-dependent bearing capacity of jacked piles in K_0 consolidated clay based on CPTU tests", *Chin. J. Geotech. Eng*., **39**(2), 193-200. https://doi.org/10.11779/CJGE201702001.

Li, L., Li, J., and Sun, D.A (2016), "Anisotropically elasto-plastic solution to undrained cylindrical cavity expansion in K0-consolidated clay", *Comput. Geotech*., **73**, 83-90. https://doi.org/10.1016/j.compgeo.2015.11.022.

Li, L., Li, J., Sun, D.A and Gong, W. (2017a), "Analysis of time-dependent bearing capacity of a driven pile in clayey soils by total stress method", *Int. J. Geomech*., **17**(7), 04016156. https://doi.org/10.1061/(ASCE)GM.1943-5622.0000860.

Li, L., Li, J., Sun, D.A. and Gong, W. (2017b), "Semi-analytical approach for time-dependent load-settlement response of a jacked pile in clay strata", *Can. Geotech. J*., **54**(12), 1682-1692. https://doi.org/10.1139/cgj-2016-0561.

Li, L., Li, J., Sun, D.A. and Gong, W. (2019), "A feasible approach to predicting time-dependent bearing performance of jacked piles from CPTu measurements", *Acta Geotechnica*, 1-18. https://doi.org/10.1007/s11440-019-00875-x.

Lim, Y.X., Tan, S. and Phoon, K. (2018), "Application of press-replace method to simulate undrained cone penetration", *Int. J. Geomech*., **18**(7), 04018066. https://doi.org/10.1061/(asce)gm.1943-5622.0001186.

Liu, H.L., Zhou, H. and Kong, G.Q. (2014), "XCC pile installation effect in soft soil ground: A simplified analytical model", *Comput. Geotech*., **62**, 268-282. https://doi.org/10.1016/j.compgeo.2014.07.007.

Liu, J.W., Zhang, Z.M., Yu, F. and Xie, Z.Z. (2012), "Case history of installing instrumented jacked open-ended piles", *J. Geotech. Geoenviron. Eng*., **138**(7), 810-820. https://doi.org/10.1061/(ASCE)GT.1943-5606.0000638.

Lorenzo, R., Cunha, R.P.D., Neto, M.P.C. and Nairn, J.A. (2016), "Numerical simulations of deep penetration problems using the material point method", *Geomech. Eng*., **11**(1), 59-76. https://doi.org/10.12989/gae.2016.11.1.059.

Lv, Y.R. and Zhang, D.D. (2018), "Geometrical effects on the load transfer mechanism of pile groups: Three-dimensional numerical analysis", *Can. Geotech. J*., **55**(5), 749-757. https://doi.org/10.1139/cgj-2016-05181.

Lv, Y.R., Liu, H.L., Ding, X.M and Kong, G.Q. (2012), "Field tests on bearing characteristics of X-section pile composite foundation", *J. Perform. Constr. Fac*., **26**(2), 180-189. https://doi.org/10.1061/(ASCE)CF. 1943-5509.0000247.

Lv, Y.R., Liu, H.L., Ng, C.W.W., Ding, X.M. and Gunawan, A. (2014a), "Three-dimensional numerical analysis of the stress transfer mechanism of XCC piled raft foundation", *Comput. Geotech*., **55**, 365-377. https://doi.org/10.1016/j.compgeo.2013.09.019.

Lv, Y.R., Liu, H.L., Ng, C.W.W., Gunawan, A. and Ding, X.M (2014b), "A modified analytical solution of soil stress distribution for XCC pile foundations", *Acta Geotechnica*, **9**(3), 529-546. https://doi.org/10.1007/s11440-013-0280-1.

Mahmoodzadeh, H., Wang, D. and Randolph, M. (2015), "Interpretation of piezoball dissipation testing in clay", *Geotechnique*, **65**(10), 831-842. https://doi.org/10.1680/jgeot.14.P.213.

Ni, P., Mangalathu, S., Mei, G. and Zhao, Y. (2017), "Permeable piles: An alternative to improve the performance of driven piles", *Comput. Geotech*., **84**, 78-87. https://doi.org/10.1016/j.compgeo.2016.11.021.

Ni, P., Mangalathu, S., Mei, G. and Zhao, Y. (2018), "Laboratory investigation of pore pressure dissipation in clay around permeable piles", *Can. Geotech. J*., **55**(9), 1257-1267. https://doi.org/10.1139/cgj-2017-0180.

Rezania, M., Mousavi Nezhad, M., Zanganeh, H., Castro, J. and Sivasithamparam, N. (2017), "Modeling pile setup in natural clay deposit considering soil anisotropy, structure, and creep effects: Case study", *Int. J. Geomech*., **17**(3), 04016075. https://doi.org/10.1061/(ASCE)GM.1943-5622.0000774.

Silvestri, V. and Abousamra, G. (2012), "Analytical solution for undrained plane strain expansion of a cylindrical cavity in modified cam clay", *Geomech. Eng*., **4**(1), 19-37. https://doi.org/10.12989/gae.2012.4.1.019.

Sun, G.C, Kong, G.Q., Liu, H.L and Amenuvor, A.C. (2017), "Vibration velocity of X-section cast-in-place concrete (XCC) pile-raft foundation model for a ballastless track", *Can. Geotech. J*., **54**(9), 1340-1345. https://doi.org/10.1139/cgj-2015-0623.

Ullah, S.N., Hou, L.F., Satchithananthan, U., Chen, Z. and Gu, H. (2018), "A 3D RITSS approach for total stress and coupled-flow large deformation problems using ABAQUS", *Comput. Geotech*., **99**, 203-215. https://doi.org/10.1016/j.compgeo.2018.01.018.

Wang, D. and Bienen, B. (2016), "Numerical investigation of penetration of a large-diameter footing into normally consolidated kaolin clay with a consolidation phase", *Geotechnique*, **66**(11), 947-952. https://doi.org/10.1680/jgeot.15.P.048.

Wang, S., Ni, P., Chen, Z. and Mei, G. (2019), "Consolidation solution of soil around a permeable pipe pile", *Mar. Georesour. Geotechnol*., 1-9. https://doi.org/10.1080/1064119X.2019.1655119.

Xu, X.T., Liu, H.L and Lehane, B.M. (2006), "Pipe pile installation effects in soft clay", *Proc. Inst. Civ. Eng. Geotech. Eng*., **159**(4), 285-296. https://doi.org/10.1680/geng.2006.159.4.285.

Yi, J.T., Lee, F.H., Goh, S.H., Zhang, X.Y. and Wu, J. (2012), "Eulerian finite element analysis of excess pore pressure generated by spudcan installation into soft clay", *Comput. Geotech*., **42**, 157-170. https://doi.org/10.1016/j.compgeo.2012.01.006.

Yi, J.T., Zhao, B., Li, Y.P., Yang, Y., Lee, F.H., Goh, S.H., Zhang. X.Y. and Wu, J. (2014), "Post-installation pore-pressure changes around spudcan and long-term spudcan behaviour in soft clay", *Comput. Geotech*., **56**, 133-147. https://doi.org/ 10.1016/j.compgeo.2012.01.006.

Zhang, D.D., Lv, Y.R., Liu, H.L. and Wang, M.Y. (2015), "An analytical solution for load transfer mechanism of XCC pile foundations", *Comput. Geotech*., **67**, 223-228. https://doi.org/10.1016/j.compgeo.2015.03.006.

Zhou, H., Liu, H.L, Yuan, J.R. and Chu, J. (2019), "Numerical simulation of XCC pile penetration in undrained clay", *Comput. Geotech*., **106**, 18-41. https://doi.org/10.1016/j.compgeo.2018.10.009.

Zhou, H., Yuan, J.R., Liu, H.L. and Kong, G.Q. (2018), "Analytical model for evaluating XCC pile shaft capacity in soft soil by incorporating penetration effects", *Soils Found*., **58**(5), 1093-1112. https://doi.org/10.1016/j.sandf.2018.04.005.

CC